Check for updates



www.chemeurj.org

# Products of the Phenyl Radical (C6H5, X2A1) – Acetylene (C2H2, $X1\Sigma g+$ ) Reaction in the 800-1,200 K Temperature Range

Oleg V. Kuznetsov, [a] Mikhail M. Evseev, [a] lakov A. Medvedkov, [a, b] Georgiy I. Tolstov<sup>†</sup>, [a] Nikolay A. Khvatov, [a] Ivan O. Antonov, [a] Ralf I. Kaiser, [b] Alexander M. Mebel, \*[c] and Valeriy N. Azyazov\*[a]

A pulsed flow high-temperature microreactor in tandem with vacuum ultraviolet photoionization (VUV PI) reflectron time-offlight mass spectrometry (Re-TOF-MS) was employed to determine branching ratios of key product channels of the reaction of the phenyl radical (C<sub>6</sub>H<sub>5</sub>) with acetylene (C<sub>2</sub>H<sub>2</sub>) highlighting the role of the Hydrogen Abstraction - C<sub>2</sub>H<sub>2</sub> Addition (HACA) mechanism at temperatures of 800-1,200 K. Temporal profiles of  $m/z = 26 (C_2H_2^+)$ , 30 (NO<sup>+</sup>), 52 (C<sub>4</sub>H<sub>4</sub><sup>+</sup>), 77 (C<sub>6</sub>H<sub>5</sub><sup>+</sup>), 78 (C<sub>6</sub>H<sub>6</sub><sup>+</sup>), 102  $(C_6H_5C_2H^+)$ , 103  $(C_6H_5C_2H_2^+)$ , 107  $(C_6H_5NO^+)$ , 128  $(C_{10}H_8^+)$ , and 154 (C<sub>12</sub>H<sub>10</sub>+) were recorded and characterized within a molecular beam. From the time profiles of the ion signals and Computational Fluid Dynamics (CFD) calculations in the transient mode, zones of the molecular beam corresponding to

the open valve duration time were identified. The gas velocity along the microreactor tube axis with the opened valve is strongly influenced by the backing pressure (p) in front of the nozzle and appears to be subsonic for p = 100 Torr and supersonic for p > 300 Torr. The main quantified finding is that phenylacetylene (C<sub>6</sub>H<sub>5</sub>C<sub>2</sub>H) constitutes the dominant product, accounting for up to 91% of consumed phenyl radicals at 1,200 K, whereas naphthalene (C<sub>10</sub>H<sub>8</sub>) formation is favored at lower temperatures and higher pressures, peaking at the yield of 53% (800 K, 300 Torr). The observed temperature and pressure dependence of naphthalene and phenylacetylene yields are consistent with the HACA mechanism.

### 1. Introduction

Polycyclic aromatic hydrocarbons (PAH) and carbon allotropes as their derivatives, such as fullerenes, bowl-shaped nanostructures, and nanoparticles (carbonaceous interstellar dust, graphene particles, soot), have garnered considerable attention from astronomers, [1] environmentalists, [2] and the combustion community.[3] Monoaromatic benzene and more complex aromatics like naphthalene (C<sub>10</sub>H<sub>8</sub>) and indene (C<sub>9</sub>H<sub>8</sub>) can grow via the addition of a new aromatic ring in diverse environments, including combustion flames,[3] the envelopes of carbon-rich asymptotic giant branch (AGB) stars, [4] and planetary nebulae. [5] Several mechanisms for PAH mass growth have been identi-

[a] O. V. Kuznetsov, M. M. Evseev, I. A. Medvedkov, G. I. Tolstov<sup>†</sup>, N. A. Khvatov, Dr. I. O. Antonov, Prof. V. N. Azyazov Combustion physics and chemistry laboratory, Samara University, Samara 443086, Russia E-mail: azvazov@rambler.ru

- [b] I. A. Medvedkov, Prof. R. I. Kaiser Department of Chemistry, University of Hawai'i at Manoa, Honolulu, HI 96822, USA
- [c] Prof. A. M. Mebel Department of Chemistry, Florida International University, Miami, Florida 33199, USA E-mail: mebela@fiu.edu
- [†] Georgiy I. Tolstov deceased February 22, 2022

Oleg V. Kuznetsov and lakov A. Medvedkov contributed equally to this work

Supporting information for this article is available on the WWW under https://doi.org/10.1002/chem.202502477

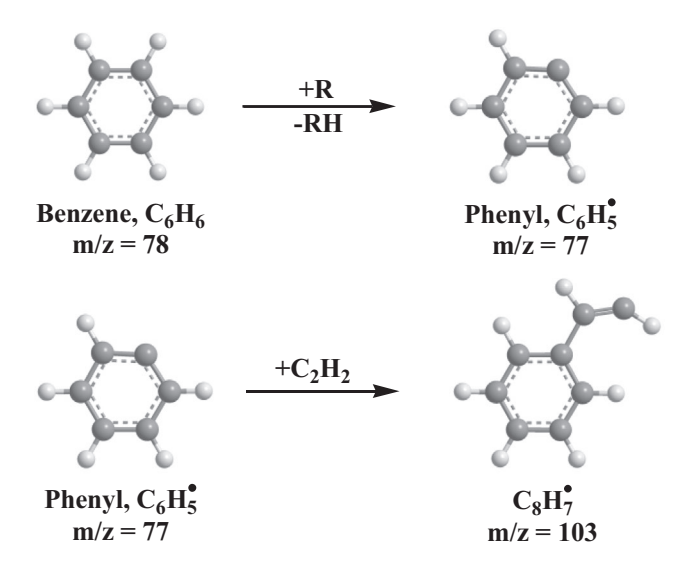


Figure 1. Formation of the primary trans-C<sub>6</sub>H<sub>5</sub>C<sub>2</sub>H<sub>2</sub> adduct.

fied experimentally, [6] among them the "Hydrogen Abstraction-Acetylene (C<sub>2</sub>H<sub>2</sub>) Addition (HACA)" mechanism.<sup>[7-9]</sup> The HACA mechanism commences with the abstraction of a hydrogen atom from benzene (C<sub>6</sub>H<sub>6</sub>) by a radical R such as hydrogen (H), hydroxyl (OH), and methyl (CH<sub>3</sub>), resulting in the formation of a phenyl radical (C<sub>6</sub>H<sub>5</sub>). Subsequently, an acetylene molecule overcomes a small energy barrier (15 kJ  $\text{mol}^{-1}\ ^{\text{[7]}}$ ), and the phenyl radical adds with its radical center to the  $\pi$  electronic system of the acetylene molecule, forming a trans-1-styrenyl radical  $(C_6H_5C_2H_2)$  (Figure 1).

ed from https://chemistry-europe.onlinelibrary.wiley.com/doi/10.1002/chem.202502477 by University Of Hawaii At Manoa, Wiley Online Library on [27/10/2025]. See the Terms and Conditions (https://onlinelibrary.wiley.com/emrs-and-conditions) on Wiley Online Library for rules of use; OA articles are governed by the applicable Cerative Commons.

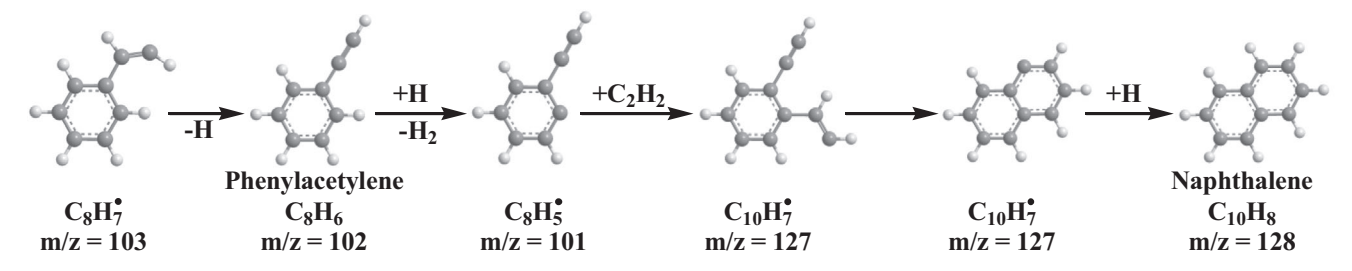


Figure 2. Frenklach route to naphthalene.

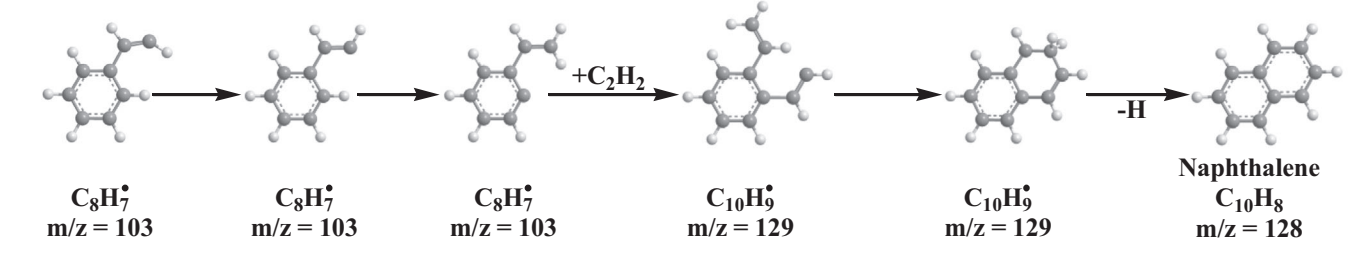


Figure 3. Bittner and Howard route to naphthalene.

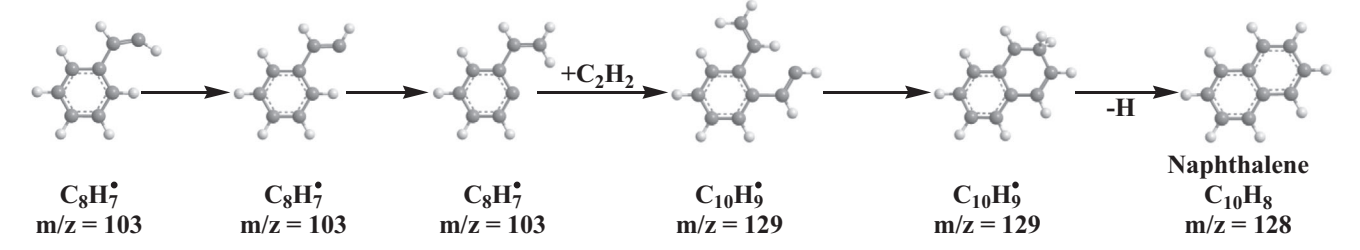


Figure 4. Modified Frenklach route to naphthalene.

Three reaction pathways leading to naphthalene originate from the  $C_6H_5C_2H_2$  adduct. Frenklach and coauthors [8-10] proposed a reaction route initiated by the loss of a hydrogen atom from the terminal carbon of C<sub>6</sub>H<sub>5</sub>C<sub>2</sub>H<sub>2</sub> yielding phenylacetylene (C<sub>6</sub>H<sub>5</sub>C<sub>2</sub>H) (Figure 2). A radical R then abstracts a hydrogen atom from the *ortho* position of the ring, forming a C<sub>6</sub>H<sub>4</sub>C<sub>2</sub>H· radical. The addition of a second acetylene molecule to this new radical site produces C<sub>6</sub>H<sub>4</sub>C<sub>2</sub>HC<sub>2</sub>H<sub>2</sub>, which readily isomerizes into the two-ring radical 1-naphthyl.[7] Finally, hydrogen addition to the radical yields the naphthalene molecule.

Two alternative pathways involve unimolecular isomerization of the primary adduct, the 1-styrenyl radical.[7,11-13] The Bittner and Howard route [11] commences with rearrangement of the primary trans adduct to a cis structure. Acetylene addition to the cis intermediate forms a 1-phenyl-but-1,3-dien-4-yl isomer (C<sub>6</sub>H<sub>5</sub>CHCHCHCH'), which readily undergoes ring closure to produce the 8a-H-naphthyl radical (C<sub>10</sub>H<sub>9</sub>·).<sup>[7]</sup> The loss of a hydrogen atom from the carbon atom bridging the two rings results in naphthalene (Figure 3).

The modified Frenklach route [12,13] involves the isomerization of the cis-1-styrenyl radical to o-vinylphenyl  $(C_6H_4C_2H_3)$ via a 1,4-H shift. Acetylene addition to the radical site forms  $C_6H_4(CHCH_2)(CHCH)$  ( $C_{10}H_9$ ), which undergoes a six-membered ring closure to yield the 2-H-naphthyl radical (C<sub>10</sub>H<sub>9</sub>·). The subsequent loss of a hydrogen atom from the CH<sub>2</sub> moiety produces naphthalene (Figure 4).

Several ab initio quantum chemistry approaches have been employed to investigate the reaction of the phenyl radical with acetylene. [7,14-17] The most comprehensive theoretical study was carried out by Mebel et al.,[7] who utilized high-level quantum chemical calculations to identify local extrema on the potential energy surface in conjunction with RRKM-Master Equation calculations to determine temperature- and pressure-dependent rate coefficients. Their findings indicate that, under typical combustion conditions at temperatures above 1,650 K, the primary trans and cis isomers of C<sub>6</sub>H<sub>5</sub>C<sub>2</sub>H<sub>2</sub> and o-vinylphenyl cannot be stabilized. Consequently, the Bittner-Howard and modified Frenklach routes contribute insignificantly, and the primary Frenklach route dominates under typical combustion conditions. However, the Bittner-Howard and modified Frenklach routes may become operative at elevated pressures above 10 atm and/or temperatures below 1,650 K.

Experimental measurements of rate constants for reactions involved in the HACA mechanism have remained limited. Fahr and Stein [18] employed a Knudsen cell flow reactor to measure the overall rate constant of the  $C_6H_5$  +  $C_2H_2$  reaction at 1000–1,330 K. Lin and coauthors  $^{[19,20]}$  determined the rate constant for the reaction of C<sub>6</sub>H<sub>5</sub> plus C<sub>2</sub>H<sub>2</sub> at 20 Torr total



pressure and temperatures ranging from 297 to 523 K using the cavity-ring-down technique. Kaiser and coauthors [21] conducted the reaction of phenyl radicals with acetylene in a resistively heated silicon carbide tube at a temperature of 1020  $\pm$  100 K analyzing the products in a molecular beam using vacuum ultraviolet (VUV) photoionization time-of-flight mass spectrometry. They detected naphthalene (C<sub>10</sub>H<sub>8</sub>) and phenylacetylene (C<sub>8</sub>H<sub>6</sub>) providing direct experimental evidence supporting the HACA mechanism. Using the same apparatus, they also investigated the reactions of 1-styrenyl and ortho-vinylphenyl radicals (C<sub>8</sub>H<sub>7</sub>')-key intermediates in the HACA mechanism-with acetylene (C<sub>2</sub>H<sub>2</sub>).<sup>[22]</sup> Naphthalene was again detected among the products, consistent with the HACA mechanism. Chu et al. [23] employed time-resolved molecular beam mass spectrometry to monitor time-dependent product formation in the C<sub>6</sub>H<sub>5</sub> plus C<sub>2</sub>H<sub>2</sub> reaction at temperatures of 600-700 K and pressures of 10-50 Torr. They observed that the contribution of the hydrogenloss branching route increases with temperature and decreases with pressure, aligning with the kinetic constants calculated by Mebel et al.[7]

An experimental validation of the HACA mechanism under combustion conditions-specifically, temperatures above 1,000 Kremains crucial. While the work of Kaiser et al.[21] provided key evidence at a single temperature (1020 K), a systematic investigation across a wider temperature and pressure range is needed to rigorously test theoretical predictions. This study presents such an investigation, measuring branching fractions for the phenyl + acetylene reaction from 800 K to 1,200 K and at pressures from 100 Torr to 600 Torr (corresponding to reactor pressures of  $\sim$ 10-100 Torr). Crucially, the pulsed operation mode of our microreactor, combined with detailed CFD analysis, provides unique mechanistic insights. By generating a short (~120 μs) gas pulse and probing its leading edge after a precise delay, we isolate a reacting packet of gas with a well-defined, short residence time. This approach effectively minimizes secondary reactions, allowing us to directly measure the nascent product branching ratios of the primary reaction steps under conditions highly relevant to combustion. Temporal and spatial profiles of relative number densities for reactants, intermediates, and products in the pulsed molecular beam in the supersonic molecular beam were determined using vacuum ultraviolet photoionization (VUV PI) reflectron time-of-flight mass spectrometry (Re-TOF-MS) with two complementary ionization methods-VUV Single Photon Ionization (VUV-SPI) and Resonantly Enhanced Multiphoton Ionization (REMPI). The VUV-SPI with 10.5 eV photons relies on its universal applicability to both closed-shell products, for example, phenylacetylene and diethynylbenzene, and radical intermediates, critical for tracking sequential HACA steps. Additionally, it uses photons with energy just above the ionization threshold of hydrocarbon combustion intermediates and nascent PAHs, enabling detection of fragile species without dissociative interference. The application of REMPI at 266 -280 nm relies on the excitation of a well-defined resonant electronic  $S_1 \leftarrow S_0$  transition at ~274 nm for selective detection of the naphthalene isomer, offering an isomer-specific sensitivity to distinguish naphthalene from its structural analogs such as azulene.

## 2. Experimental and computational

#### 2.1. Experimental Setup

The experiments were conducted in the Combustion Physics and Chemistry Laboratory at Samara National Research University in a molecular beams machine. The schematic view of the experimental setup is illustrated in Figure 5. The apparatus comprises a vacuum system constructed from 304 L stainless steel featuring a main chamber and a source chamber with dimensions of 120 cm  $\times$  120 cm  $\times$  70 cm, that is, close to 1000 L volume. The vacuum system is evacuated by magnetically levitated turbomolecular pumps (Osaka TG2400M, 2000 L/s for the main and source chambers; Osaka TG420M, 420 L/s for the ReTOF chamber), supported by a dry scroll pump (Edwards XDS35iC, 10 L/s). This oil-free vacuum system achieves base pressures in the range of  $10^{-7}$  to  $10^{-9}$  Torr, depending on the gas load during experiments.

The source chamber is equipped with a piezoelectric Proch-Trickl pulsed valve [24] (1 mm nozzle diameter) driven by-400 V pulses with an 80 µs duration and producing gas pulses with a duration of approximately 120 µs. The gas pulses are directed through a 3 cm long, 1 mm internal diameter Al<sub>2</sub>O<sub>3</sub> tube, which is resistively heated using a molybdenum wire. The heated zone, located near the tube exit, is maintained at a controlled temperature monitored by a type K thermocouple. The wire turn pitch was chosen to ensure a uniform wall temperature distribution in the reaction zone. The length of the heated zone is optimized to ensure a short residence time, thereby focusing on primary chemical processes and minimizing secondary reactions among the products. Upon exiting the tube, the gas undergoes adiabatic expansion into the vacuum, forming a molecular beam after passing through a 1 mm conical skimmer. A detailed description of the microreactor and typical temperature profiles is presented in the Supporting Information. The molecular beam enters the main chamber, which houses a reflectron timeof-flight mass spectrometer (Re-TOF-MS, Jordan TOF Products). In the ionization region of the Re-TOF-MS, the beam intersects with a photoionization laser pulse, which ionizes the molecules of interest. Two photoionization schemes were employed: single photon VUV ionization at 118 nm (10.5 eV) and resonanceenhanced multiphoton ionization (REMPI) at 278.5 nm.

## 2.2. VUV Photoionization

The 118 nm VUV radiation is generated via third-harmonic generation of 355 nm light from an Nd:YAG laser (Spectra Physics Quanta-Ray PRO-290–10E; 10 ns pulse duration; 10 Hz repetition rate; 2–7 mJ/pulse). These 10.5 eV photons enable soft single-photon ionization, minimizing fragmentation while efficiently ionizing critical reaction intermediates and products. Here, the 355 nm beam is focused into the center of a tripling cell using a lens with a 50 cm focal length. The cell is filled with a 1:11 mixture of xenon (Xe) and argon (Ar), which provides phase matching for efficient third-harmonic generation. [25] The gas pressure ratio

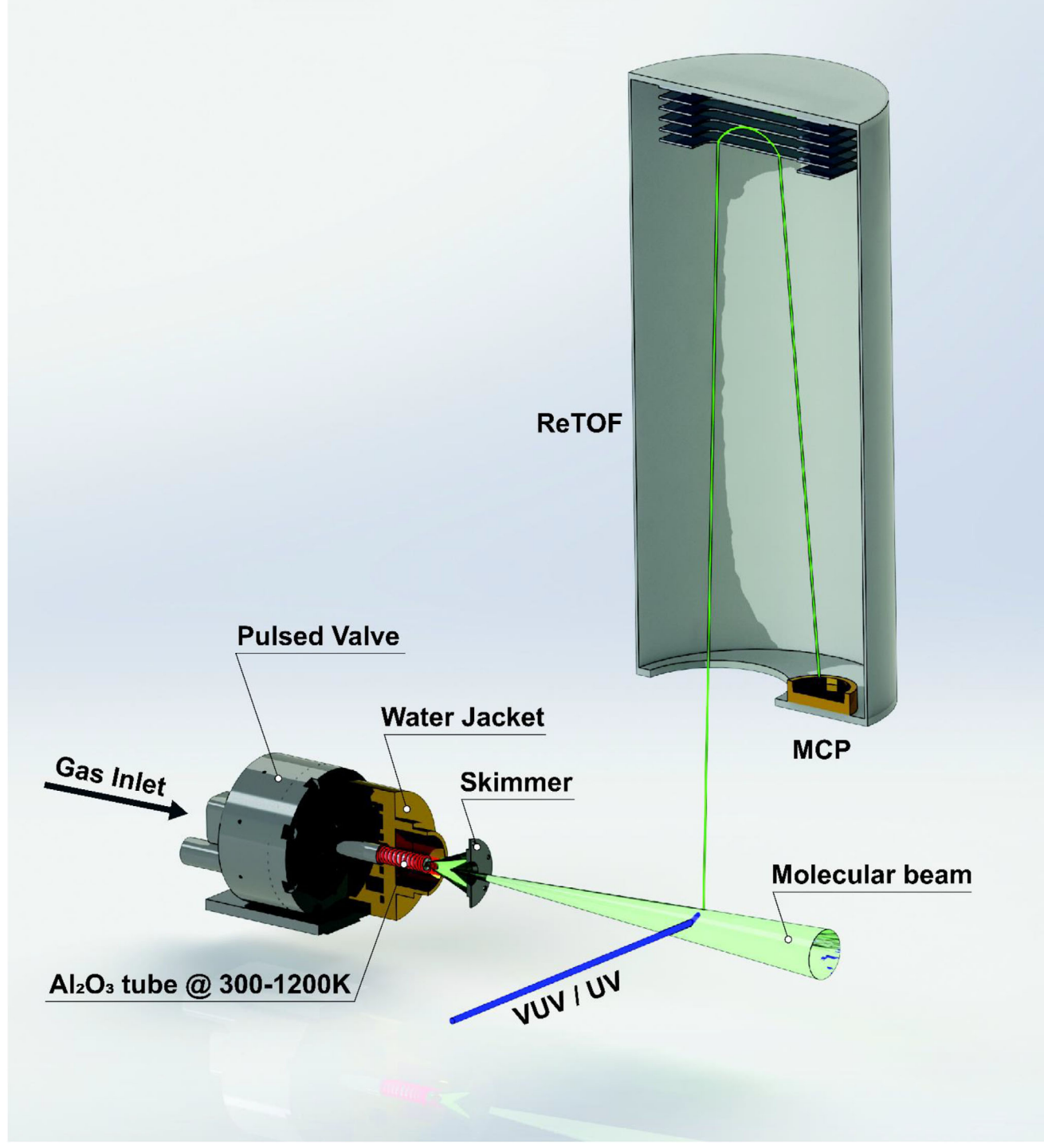


Figure 5. 3D CAD model of the experimental setup. The setup includes a high-temperature aluminum oxide (Al<sub>2</sub>O<sub>3</sub>) microreactor with a molybdenum wire heating element, a pulsed valve for gas injection, a vacuum chamber for gas expansion, and a photoionization Re-TOF-MS mass spectrometer for product detection.

in the cell is monitored via a capacitance manometer (ATO-VAC ACM200). The resulting VUV light is separated from the 355 nm radiation using a 20 cm magnesium fluoride (MgF<sub>2</sub>) lens and focused into the ionization region of the Re-TOF-MS. The fluence of the 118 nm light is monitored using a custombuilt Faraday cup detector positioned behind the ionization region.

#### 2.3. REMPI Photoionization

For Resonantly Enhanced Multiphoton Ionization (REMPI) experiments, tunable UV light near 278.5 nm is produced by frequency doubling the output of a Sirah PrecisionScan dye laser operating with Coumarin 153 dye. This wavelength is precisely tuned to resonate with the  $S_1 \leftarrow S_0$  electronic transition of naphthalene, and-conditions) on Wiley Online Library for rules of use; OA articles are governed by the applicable Creative Commons



ensuring high selectivity for its detection and discrimination against isomeric species such as azulene. The laser pulse energy is measured using an Ophir LaserStar-D power meter equipped with a PE25-C pyroelectric head. In both VUV and REMPI experiments, the relative fluence of the laser pulses is recorded and used to normalize the signal intensity.

#### 2.4. Ion Detection and Analysis

Following photoionization, the resulting cations are accelerated by the voltage difference of 1,200 V between the ion source electrodes and are extracted into the field-free flight tube of the Re-TOF-MS. An ion mirror at the end of the flight tube reflects the ions, providing second-order mass focusing. The ions are detected by a 40 mm microchannel plate (MCP) detector positioned 76 mm downstream of the photoionization point along the molecular beam axis, near the flight tube entrance. (Figure 5). The signal from the MCP is amplified using an Ortec 9306 preamplifier, discriminated with an F-100TD discriminator (Advanced Research Instruments Corporation), and recorded using an MCS6A Fast ComTec multiscaler. The Re-TOF-MS achieves a mass resolution (M/ $\Delta$ M) of approximately 600, sufficient to fully resolve mass peaks of hydrocarbon species within the target mass range of 12–160 atomic mass units (amu).

#### 2.5. Gas Mixture and Experimental Conditions

The gas mixture comprised acetylene (99% purity), which functioned as both the carrier gas and the precursor of the reactant. Here, to generate phenyl radicals, nitrosobenzene (C<sub>6</sub>H<sub>5</sub>NO) vapor was introduced into the system as a precursor. This was achieved by flowing the acetylene carrier gas over a bed of nitrosobenzene powder (97% purity, Sigma Aldrich) housed in a temperature-controlled vessel (stainless steel bubbler) maintained at 273 K by means of an ice bath. Under these conditions, the nitrosobenzene reached a stable vapor pressure of 0.33 Torr, [26] ensuring consistent delivery of the precursor to the reaction zone via the pulsed valve. Experiments were conducted at backing pressures of p = 100, 300, and 600 Torr, with wall temperatures of the microreactor ranging from 800 to 1,200 K in steps of 100 K. Both VUV and REMPI photoionization schemes were employed for studies of the reaction. Additionally, reference studies were conducted at 300 K for each pressure using only VUV photoionization. The operation of the pulsed valve, Nd:YAG laser, and data acquisition system was synchronized using a Quantum Composer 9528 pulse delay generator. Time-resolved mass spectra were obtained by systematically varying the delay between the opening of the pulsed valve and the arrival of the ionization laser pulse. This approach allowed for probing different regions of the gas pulse, with shorter delays corresponding to the leading edge and longer delays to the trailing edge. The time step for each measurement was 5 µs over a 500 µs window. Signal averaging was performed over 3000 laser pulses for VUV experiments (5 minutes at 10 Hz) and 1200 pulses for REMPI experiments (2 minutes at 10 Hz).

#### 2.6. Computational Fluid Dynamics (CFD) Simulations

The analysis of experimental data necessitates a comprehensive understanding of key reactor conditions, including temperature, pressure, and residence time. In the present study, direct measurement of these parameters as a function of position within the reactor tube and time during the gas pulse was experimentally infeasible. Therefore, time-dependent computational fluid dynamics (CFD) simulations of the microreactor were employed to quantify these conditions for all backing pressures and wall temperatures utilized in the experiments. Compared to previous simulations, which operated with a continuous flow, [27,28] the present simulations account for the pulsed nature of the gas pulse. These CFD simulations incorporated the reactor geometry, gas pulse dynamics, wall temperature profile, gas mixture composition, and inlet/outlet pressures as boundary and initial conditions. The simulations captured the propagation of the gas pulse through the reactor and its expansion into high vacuum, spanning both the open-valve period (active gas injection) and the post-closure phase (residual gas dynamics). A comprehensive description of the CFD methodology is provided in the Supporting Information.

The CFD simulations mapped the temporal and spatial evolution of temperature, pressure, and flow dynamics within the reactor, which was crucial for accurately interpreting the experimental data. The mean residence time was computed by tracking the time delay for equivalent cumulative mass flows to cross the inlet and outlet of the heated zone. This CFD-derived result agreed well with an independent estimate based on the molecular beam's time-of-flight (200–300  $\mu s$ ) and the length ratio of the heated zone ( $\approx\!0.14$ ). These derived conditions, summarized in Table 1 as functions of tube temperature (T) and backing pressure (p), provide the framework for our kinetic analysis.

**Table 1.** Computed residence time, acetylene number density, and average temperature in the microreactor's heated zone as a function of temperature (T) and pressure (p), obtained from CFD simulations.

Temperature [K]	100 Torr	300 Torr	600 Torr
800	62 μs, 5.84·10 <sup>16</sup> cm <sup>-3</sup> 798 K	44 μs, 4.45·10 <sup>17</sup> cm <sup>-3</sup> 624 K	
900	63 $\mu$ s, 5.41·10 <sup>16</sup> cm <sup>-3</sup> 908 K	44 μs, 4.27·10 <sup>17</sup> cm <sup>-3</sup> 717 K	
1000	63 μs, 4.94·10 <sup>16</sup> cm <sup>-3</sup> 1012 K	44 μs, 4.10·10 <sup>17</sup> cm <sup>-3</sup> 815 K	41 μs, 1.10·10 <sup>18</sup> cm <sup>-3</sup> 670 K
1100	62 μs, 4.42·10 <sup>16</sup> cm <sup>-3</sup> 1116 K	43 μs, 3.85·10 <sup>17</sup> cm <sup>-3</sup> 919 K	41 μs, 1.06·10 <sup>18</sup> cm <sup>-3</sup> 749 K
1200	62 $\mu$ s, 4.04·10 <sup>16</sup> cm <sup>-3</sup> 1212 K	43 μs, 3.70·10 <sup>17</sup> cm <sup>-3</sup> 1022 K	



#### 3. Results and Discussion

# 3.1. Comparative Mass Spectrometry of Reacted Mixtures and Background

Figure 6 displays a representative mass spectrum of the reaction products obtained at 1,000 K and 300 Torr. A complete dataset of mass spectra for all investigated pressure and temperature conditions is provided in the Excel file in the Supporting Information. The primary pyrolysis and reaction products were identified in the following mass-to-charge ratio (m/z) channels: 30 (NO+), 52 (C $_4$ H $_4$ +), 77 (C $_6$ H $_5$ +), 78 (C $_6$ H $_6$ + and the  $^{13}$ C isotopologue of  $C_6H_5^+$ ), 102 ( $C_8H_6^+$ ), 103 ( $C_8H_7^+$  and the  $^{13}C$ isotopologue of  $C_8H_6^+$ ), and 128 ( $C_{10}H_8^+$ ). Peaks corresponding to the reactants were also observed including, acetylene (m/z = 26) and the phenyl radical precursor nitrosobenzene ( $C_6H_5NO$ , m/z = 107); no higher mass peaks originating from products than m/z = 128 were observed. Notably, acetylene (ionization potential, IP = 11.4 eV) should not be ionized by a single 10.5 eV VUV photon. The signal at m/z = 26 is therefore likely due to multiphoton ionization and/or electron-impact ionization from stray VUV-generated electrons ejected from the ion optics and accelerated by the ion extraction field. Several minor hydrocarbon peaks were detected, attributable to trace products or carrier gas impurities: 28  $(C_2H_4^+)$ , 39  $(C_3H_3^+)$ , 40  $(C_3H_4^+)$ , 42  $(C_3H_6^+)$ , 50  $(C_4H_2^+)$ , 56  $(C_4H_8^+)$ , 65  $(C_5H_5^+)$ , 66  $(C_5H_6^+)$ , 123  $(C_6H_5NO_2^+$ , nitrobenzene impurity in the precursor).

Among these, ethylene (m/z=28) was particularly prominent in the top trace but absent in the bottom trace. Since it was also detected in a blank acetylene spectrum at 1,000 K (Figure S6 Supporting Information), its presence is attributed to carrier gas impurities rather than reaction products. The observed signal intensity variation is consistent with the temperature-dependent ionization cross-section of ethylene near the ionization threshold at 10.5 eV. Semi-quantitative analysis indicates that the concentration of ethylene is significantly lower than that of acetylene and shows no evidence of  $C_2H_4$  consumption, confirming that it does not participate in chemistry competitive with the phenyl + acetylene reaction. For clarity, the subsequent discussion focuses exclusively on primary reaction products, as minor species are assumed not to influence the dominant chemical pathways.

#### 3.2. Time-Dependent Behavior of Key Species

The left panel of Figure 7 presents the time-dependent profiles of mass peaks of  $C_2H_2^+$  (acetylene, m/z=26),  $NO^+$  (nitrogen monoxide, m/z=30), and  $C_6H_5NO^+$  (nitrosobenzene, m/z=107) recorded at 1,000 K under pressures of p=100, 300, and 600 Torr.

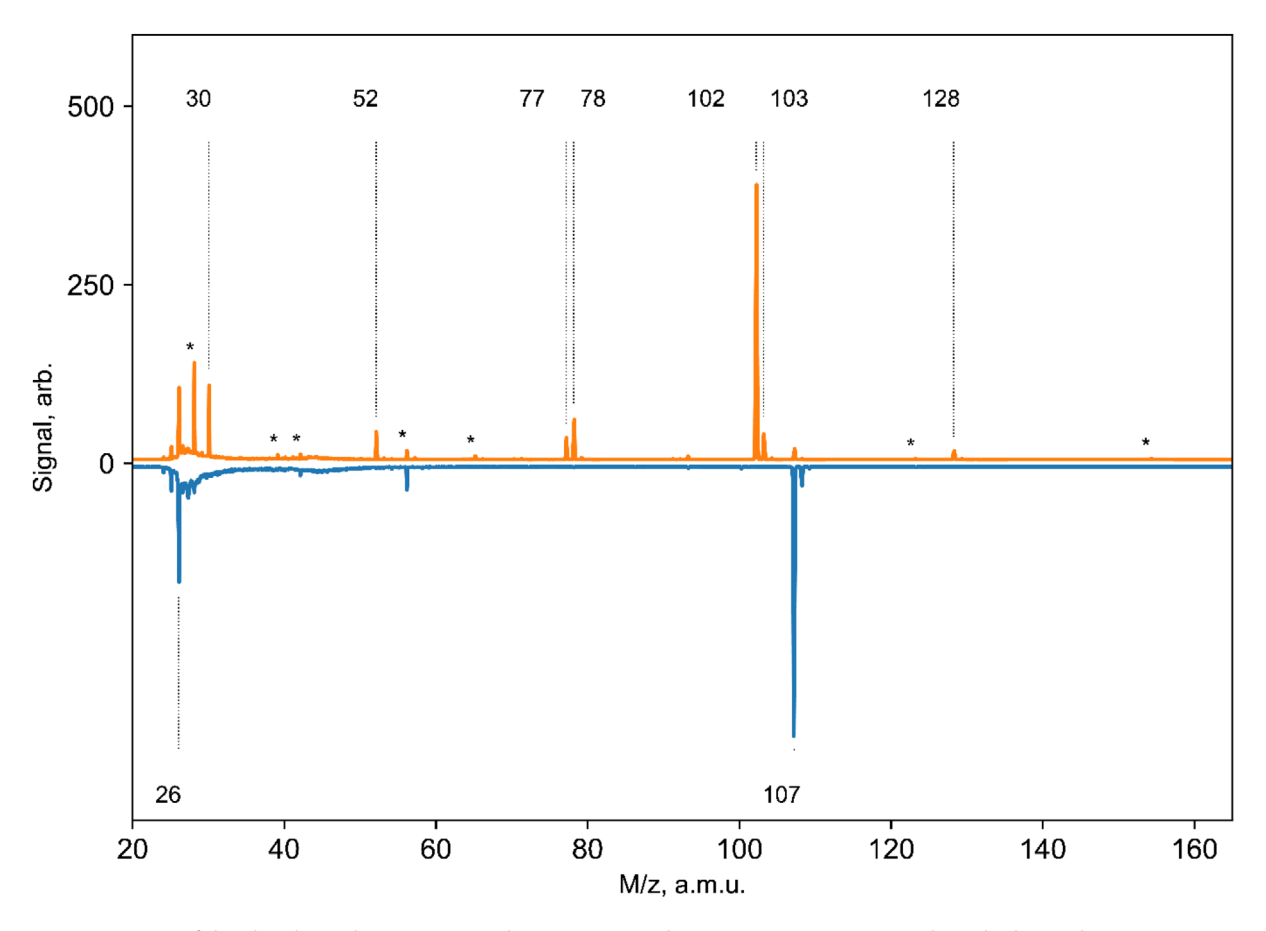


Figure 6. Mass spectrum of the phenyl-acetylene reaction products at 1000 K and 300 Torr (top trace) compared to a background spectrum at 300 K and 300 Torr (bottom trace). Primary reactants and products are labeled with their corresponding mass-to-charge ratios (m/z). Impurities and minor products are marked with asterisks (\*).

Chemistry Europe

European Chemical Societies Publishing

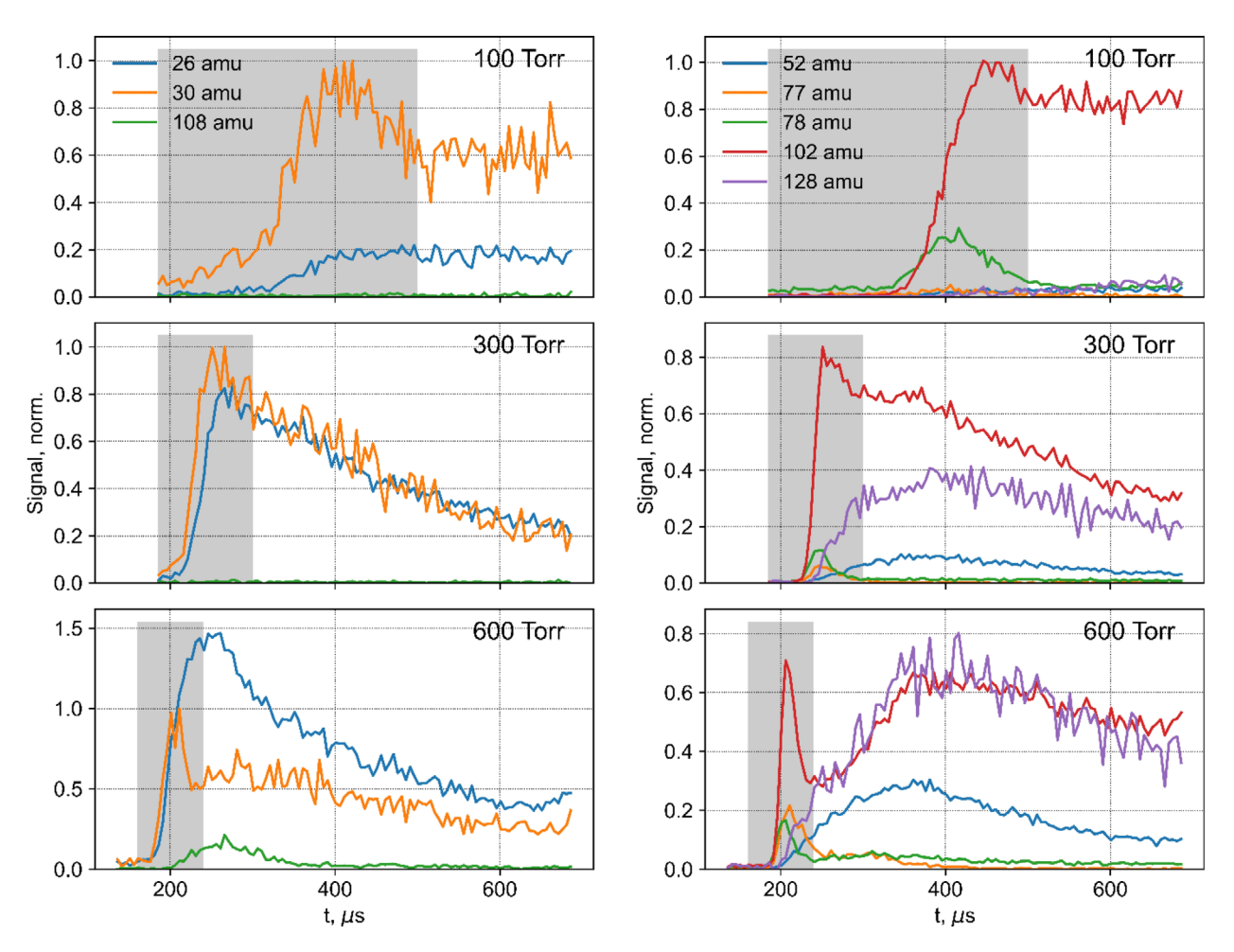


Figure 7. Temporal evolution of reactant and product signals in the pyrolysis of nitrosobenzene/acetylene mixtures at 1,000 K. The time t=0 is defined as the instant when the valve begins to open. Left panel: Time-resolved mass spectra of  $C_2H_2^+$  (m/z=26),  $NO^+$  (m/z=30), and  $C_6H_5NO^+$  (m/z=107) at  $p = 100, 300, \text{ and } 600 \text{ Torr. } \text{Right panel}: \text{Time-dependent profiles of major products: } C_4H_4^+ (m/z = 52), C_6H_5^+ (m/z = 77), C_6H_6^+ (m/z = 78), C_8H_6^+ (m$ (m/z = 102), and  $C_{10}H_8^+$  (m/z = 128), highlighting pressure-dependent kinetics and secondary chemistry. Integration windows for yield analysis (gray boxes): 250-500 μs (100 Torr), 185-300 μs (300 Torr), and 160-240 μs (600 Torr).

The time profiles of the signals are normalized to the NO signal as described below. The time origin (t = 0) is defined as the instant when the valve begins to open. Given the absence of reaction channels for NO at our experimental conditions and the vast excess of acetylene relative to nitrosobenzene, their temporal trends primarily reflect the hydrodynamic behavior of the gas pulse. The onset of the NO and C2H2 signals corresponds to the arrival time of the leading edge of the gas pulse to the photoionization point. The time-to-maximum for the NO signal decreases systematically with increasing pressure, occurring at 500 μs (100 Torr), 240 μs (300 Torr), and 200 μs (600 Torr), demonstrating both pulse acceleration and narrowing of the relative velocity distribution at higher pressures.

Gas flow parameters in a high-temperature microreactor operating in continuous mode have been investigated in a number of papers. [27-29] No attempts have been made to characterize the pulsed flow of gas with variable flow rate in a chemical microreactor due to its complexity. In this work, the measured temporal profiles of relative number densities of components in a pulsed molecular beam were taken into account to extract gas-dynamic characteristics of the flow in a microreactor. Temporal profiles of acetylene signals (Figure 7, Left Panel) illustrate that gas pressure increases during the entire opening time of the pulse valve (60 msec) due to the increase in gas flow rate. As the valve starts to close, the signal drops, but the rate of decline is noticeably weaker. After the valve is completely closed, the gas remaining in the channel gradually flows out for a long time.

Figure 7 reveals that at a backing pressure of 100 Torr, the gas pulse front takes approximately 320 us to travel from the pulse valve to the ionization point (distance = 11.5 cm). This corresponds to an average flow velocity near the tube axis that approaches the speed of sound in acetylene. In contrast, at higher backing pressures (300-600 Torr), the observed travel time indicates supersonic flow, both within the microreactor and during the subsequent molecular beam expansion. At a backing pressure of 600 Torr with laser delay times larger than 20 μs from the leading edge of the gas pulse, the increased gas density leads to a significant temperature drop along the flow axis compared to the microreactor wall temperature. This thermal gradient is clearly demonstrated by the signal profiles in Figure 7 (p = 600 Torr). In the high-pressure regime, the nitrosobenzene signal intensity increases due to suppressed pyrolysis at



the cooler flow axis (left panel). Concurrently, the NO signal decreases, leading to reduced phenylacetylene production rates (right panel). Following valve closure, the extended gas residence time in the reactor allows complete thermal equilibration with the wall temperature, resulting in the recovery of all signal intensities.

The right panel of Figure 7 tracks the time-dependent profiles of mass peaks of major reaction products:  $C_4H_4^+$  (m/z=52),  $C_6H_5^+$  (phenyl radical, m/z=77),  $C_6H_6^+$  (m/z=78),  $C_8H_6^+$  (phenylacetylene, m/z=102), and  $C_{10}H_8^+$  (naphthalene, m/z=128). At p=100 Torr, the  $C_6H_5^+$  signal peaks at 400  $\mu$ s, mirroring the NO<sup>+</sup> temporal profile, while the  $C_8H_6^+$  product (m/z=102) displays a 50  $\mu$ s delay. Elevated pressures (300–600 Torr) produce a more complex behavior: the m/z=77 and 78 signals remain synchronized with NO, whereas m/z=102 exhibits a 5–10  $\mu$ s lag and develops a sharp feature (225–300  $\mu$ s at 300 Torr; 190–240  $\mu$ s at 600 Torr) followed by signal depletion and gradual recovery.

In contrast,  $C_4H_4$  (m/z=52) and naphthalene (m/z=128) demonstrate distinctly different kinetics, with signals rising monotonically throughout the pulse duration and peaking in the tail region. This delayed evolution suggests their formation stems from slower reactions or secondary chemistry (higherorder product formation) involving primary products generated earlier in the pulse—particularly  $C_8H_6$  (m/z=102), which appears as a sharp feature preceding the  $C_4H_4$  and  $C_{10}H_8$  maxima. The temporal decoupling implies sequential reactions where  $C_8H_6$  and coproduced hydrogen atoms serve as intermediates for downstream pathways.

Hence, the temporal data reveal a complex pressure-dependent chemical behavior coupled to fluid dynamics. At 100 Torr, rapid thermal equilibration ensures complete nitrosobenzene dissociation and subsequent phenyl radical chemistry. For higher pressures (300–600 Torr), the leading edge of the gas pulse achieves sufficient temperature for efficient nitrosobenzene pyrolysis and fast phenyl-acetylene reactions, while the denser core experiences attenuated heating, resulting in incomplete precursor decomposition and retarded product formation. This thermal gradient creates the observed product-specific timing offsets and signal modulation.

For a quantitative analysis, we focus on the entire gas pulse duration at 100 Torr (250–500  $\mu$ s) and the leading edge at elevated pressures (185–300  $\mu$ s at 300 Torr; 160–240  $\mu$ s at 600 Torr). The time gates are shown as the gray areas in Figure 7; they were used for signal integration in the relative yield calculations. This selective time-gating isolates regions with well-defined thermal histories and residence times, as the nominal pre-expansion pressures (100–600 Torr) are not conserved during pulse propagation through the reactor. This approach ensures that yield estimates reflect conditions where temperature and reaction kinetics are spatially and temporally uniform, minimizing artifacts from the colder and denser gas in the pulse head as well as from the hotter trailing portions with much longer residence times.

Neither the original nor the modified HACA mechanisms include reaction pathways capable of explaining the observed

formation of m/z=78 ( $C_6H_6$ ), 52 ( $C_4H_4$ ), and 154 ( $C_{12}H_{10}$ ) species in our experiments. The signal at m/z=52 can be attributed to reactions between vinyl radicals ( $C_2H_3$ \*) and acetylene ( $C_2H_2$ ) followed by hydrogen atom loss as previously reported by Smith et al.<sup>[30]</sup> The vinyl radicals may be generated via addition of hydrogen atoms. The potential energy surface for the reaction between vinyl and acetylene features a 27 kJ mol<sup>-1</sup> entrance barrier and was shown [31] to proceed with a rate constant of  $k=1.47\times 10^{-13}$  cm<sup>3</sup>/s at 980 K, which translates into a characteristic time of  $\tau=(k\ [C_2H_2])^{-1}\approx 140\ \mu s$  for our typical conditions (T = 1,000 K, p=300 Torr and  $[C_2H_2]=4.94\times 10^{16}$  cm<sup>-3</sup> (Table 1). This value agrees well with the observed temporal behavior of m/z=52 signal, which builds up at a time delay of  $>100\ \mu s$  after the signal onset.

While the formation of benzene ( $C_6H_6$ , m/z=78) and biphenyl ( $(C_6H_5)_2$ , m/z=154) could result from phenyl radical ( $C_6H_5$ ') recombination with atomic hydrogen and itself, respectively, quantitative analysis contradicts this hypothesis under our experimental conditions. The large excess of acetylene should kinetically favor reactions of both phenyl radicals and atomic hydrogen and acetylene over radical recombination pathways. The mechanisms underlying benzene and biphenyl formation thus warrant further investigation beyond the scope of this study. Consequently, our discussion hereafter focuses exclusively on products generated via the phenyl/acetylene reaction through established HACA mechanisms.

## 3.3. Quantification of Phenyl-Derived Product Yields

The relative yields of phenyl-derived products presented in Figure 8 were determined by integrating their time-resolved signal profiles over selected time windows, as described in the preceding section. For each product i, the yield  $Y_i$  was calculated according to:

$$Y_{i} = N \frac{\int S_{i}(t) dt}{\sigma_{i} \mu_{i}}, \tag{1}$$

where  $S_i(t)$  represents the time-dependent signal intensity,  $\sigma_i$ denotes the photoionization cross-section at 10.5 eV, and  $\mu_i$ is a mass-discrimination correction factor caused mainly by a stronger displacement of the landing site of heavy mass ions along the molecular beam coordinate. The normalization constant  $N = \sum_i Y_i$  scales the yields to the total observed phenylderived product concentration, ensuring consistency across measurements. Photoionization cross-sections at 10.5 eV were assigned based on established literature values: 28.8 Mb for the phenyl radical ( $C_6H_5$ , m/z = 77), 62.82 Mb for phenylacetylene ( $C_8H_6$ , m/z = 102), and 51.18 Mb for naphthalene  $(C_{10}H_8, m/z = 128)$ . These values account for differences in detection efficiency due to variations in ionization probability. To correct for mass-dependent detection biases, the mass-discrimination factors  $\mu_i$  were determined by enforcing mass balance between the integrated signal of NO and the sum of phenyl-derived products, normalized by their respective

5213765, 20

59, Downloaded from https://chemisty-europe.onlinelibrary.wiley.com/doi/10.1002/chem.202502477 by University Of Hawaii At Manoa, Wiley Online Library on [27/10/2025]. See the Terms and Conditions (https://onlinelibrary.wiley.com/terms-and-conditions) on Wiley Online Library for rules of use; OA articles are governed by the applicable Creative Commons

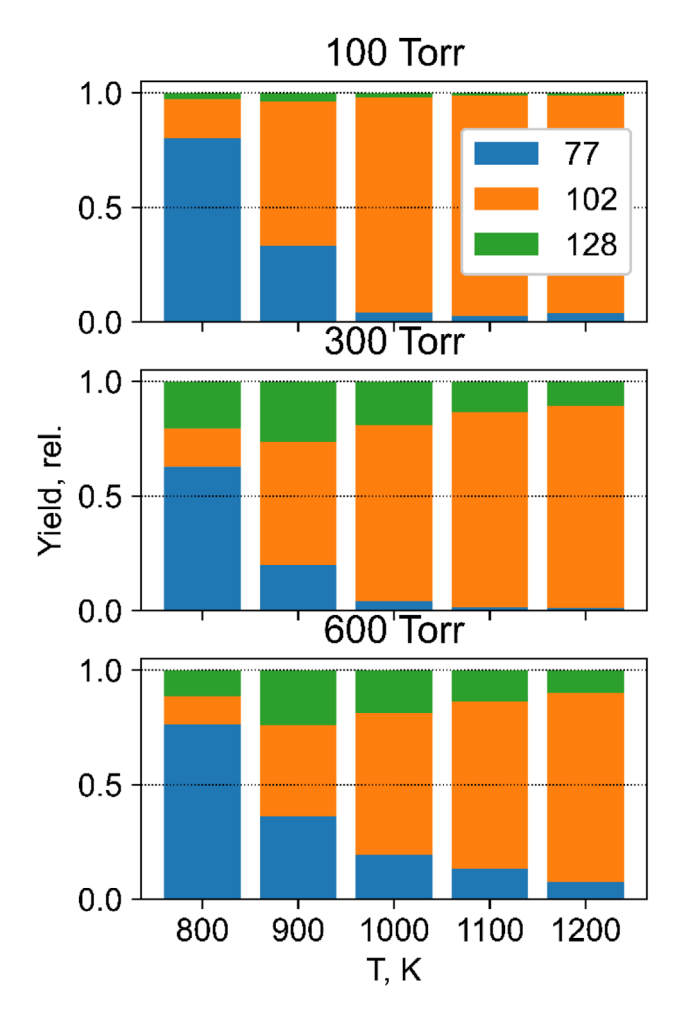


Figure 8. Temperature-dependent relative yields of phenyl-derived products formed in the reaction of phenyl radicals with acetylene at p = 100 Torr (top), 300 Torr (middle), and 600 Torr (bottom). Bar colors represent different products: phenyl radical (C<sub>6</sub>H<sub>5</sub><sup>-</sup>, 77 amu, blue), phenylacetylene (C<sub>8</sub>H<sub>6</sub>, 102 amu, orange), and naphthalene (C<sub>10</sub>H<sub>8</sub>, 128 amu, green). The height of each bar corresponds to the normalized product yield.

cross-sections:

$$\frac{\int S_{NO}(t) dt}{\sigma_{NO} \mu_{NO}} = \sum_{i} \frac{\int S_{i}(t) dt}{\sigma_{i} \mu_{i}} . \tag{2}$$

Here  $\mu_i$  was modeled as a 2-parameter Gaussian function of molecular mass:

$$\mu_{i} = \exp\left(-0.5\left(\frac{(\mathsf{m}_{i} - \mathsf{m}_{0})}{\mathsf{w}}\right)^{2}\right),\tag{3}$$

where  $m_i$  is the mass of species i (or NO), and  $m_0$  and ware fitted parameters representing the center and width of the mass-dependent correction. These parameters were optimized separately for each pressure condition but remained fixed across all temperatures at a given pressure, which was justified by the observed pressure and temperature dependencies of the gas pulse temporal shapes.

The temperature-dependent product yield distributions suggest distinct reaction pathways for phenyl radicals in the presence of acetylene. At 800 K, the majority of phenyl radicals remain unreacted within the reactor residence time, indicating minimal reactivity in the low-temperature regime.

With increasing temperature, phenyl radicals, which reacted with acetylene (quantified by  $\Delta Y_{77} = 1 - Y_{77}$ ) primarily form two products: phenylacetylene ( $C_6H_5C_2H\ m/z=102$ ) and naphthalene ( $C_{10}H_8$ , m/z = 128). Figure 8 reveals clear temperatureand pressure-dependent trends. The phenylacetylene yield  $(\gamma_{128} = Y_{128}/\Delta Y_{77})$  shows strong temperature dependence, increasing from about 47% at 800 K to nearly 91% at 1,200 K, establishing its dominance at higher temperatures. The naphthalene yield ( $\gamma_{102} = Y_{102}/\Delta Y_{77}$ ) at 300 Torr decreases progressively from 53% (800 K) to 10% (1,200 K), indicating deteriorating conditions for ring-formation kinetics with temperature elevation. At 100 Torr, the maximum naphthalene yield (about 10%) occurs at the lowest temperature, remaining below a few percent at higher temperatures. The pressure dependence (Figure 8) shows enhanced naphthalene formation at higher pressures. These observed trends align with the HACA mechanism. At elevated temperatures, the original HACA pathway dominates, favoring phenylacetylene formation. Conversion to naphthalene via the Frenklach route is suppressed because (i) temperatures are insufficient for thermal H-loss from phenylacetylene, and (ii) H-atoms (required for H-abstraction) are rapidly consumed in the side reaction (2). Thus, observed naphthalene primarily forms under high-pressure, low-temperature conditions, when the C<sub>8</sub>H<sub>7</sub> (C<sub>6</sub>H<sub>5</sub>C<sub>2</sub>H<sub>2</sub>) adduct stabilizes, activating the alternative HACA pathways. Under our experimental conditions ( $p \approx 10$ – 100 Torr; T = 1,000 K; reaction time:  $\tau = 45-65 \mu s$ ), phenyl radicals generated from nitrosobenzene pyrolysis primarily yield phenylacetylene. A representative case at p=100 Torr and 1,000 K ( $\tau$ = 63  $\mu$ s,  $[C_2H_2] = 4.94 \times 10^{16} \text{ cm}^{-3}$  (Table 1) yields a pseudo firstorder rate coefficient of  $k = (\tau \ [C_2H_2])^{-1} \approx 3 \times 10^{-13} \ cm^3/s$  for the reaction  $C_6H_5^* + C_2H_2 \rightarrow \textit{products}$ . This value shows good agreement with theoretical calculations, for example,  $4.9 \times 10^{-13}$ cm<sup>3</sup>/s at 1,000 K and 30 Torr,<sup>[7]</sup> confirming the reliability of our experimental methodology.

Figure 9 exhibits selected temporal profiles of m/z = 128signal detected with two photoionization schemes: VUV ionization at 118 nm and resonance-enhanced multiphoton ionization (REMPI) near 278.5 nm to gain insight into the isomeric composition of the m/z = 128 product. A noticeable difference is observed only for a pressure of p = 600 Torr and temperatures above 1,000 K and at times after the valve is closed. Under these conditions, high number densities of vinylacetylene are also observed (Figure 7). It can be concluded that under these conditions, a distinct set of one-ring aromatic compounds (1- and/or 4-phenylvinylacetylene,  $(C_6H_5(CH)_2C_2H / C_6H_5C_2C_2H_3,$ C<sub>10</sub>H<sub>8</sub>), isomeric to naphthalene, is produced by the hydrogen abstraction-vinylacetylene addition (HAVA) mechanism, [21,35] which contributes to the m/z=128 signal obtained with VUV ionization but is invisible for the REMPI ionization, which used 278.5 nm light in resonance with the naphthalene electronic transition.

5213765, 20

ded from https://chemistry-europe.onlinelibrary.wiley.com/doi/10.1002/chem.202502477 by University Of Hawaii At Manoa, Wiley Online Library on [27/10/2025], See the Terms and Conditions (https://onlinelibrary.wiley.com/terms-and-conditions) on Wiley Online Library for rules of use; OA articles are governed by the applicable Certaive Commons

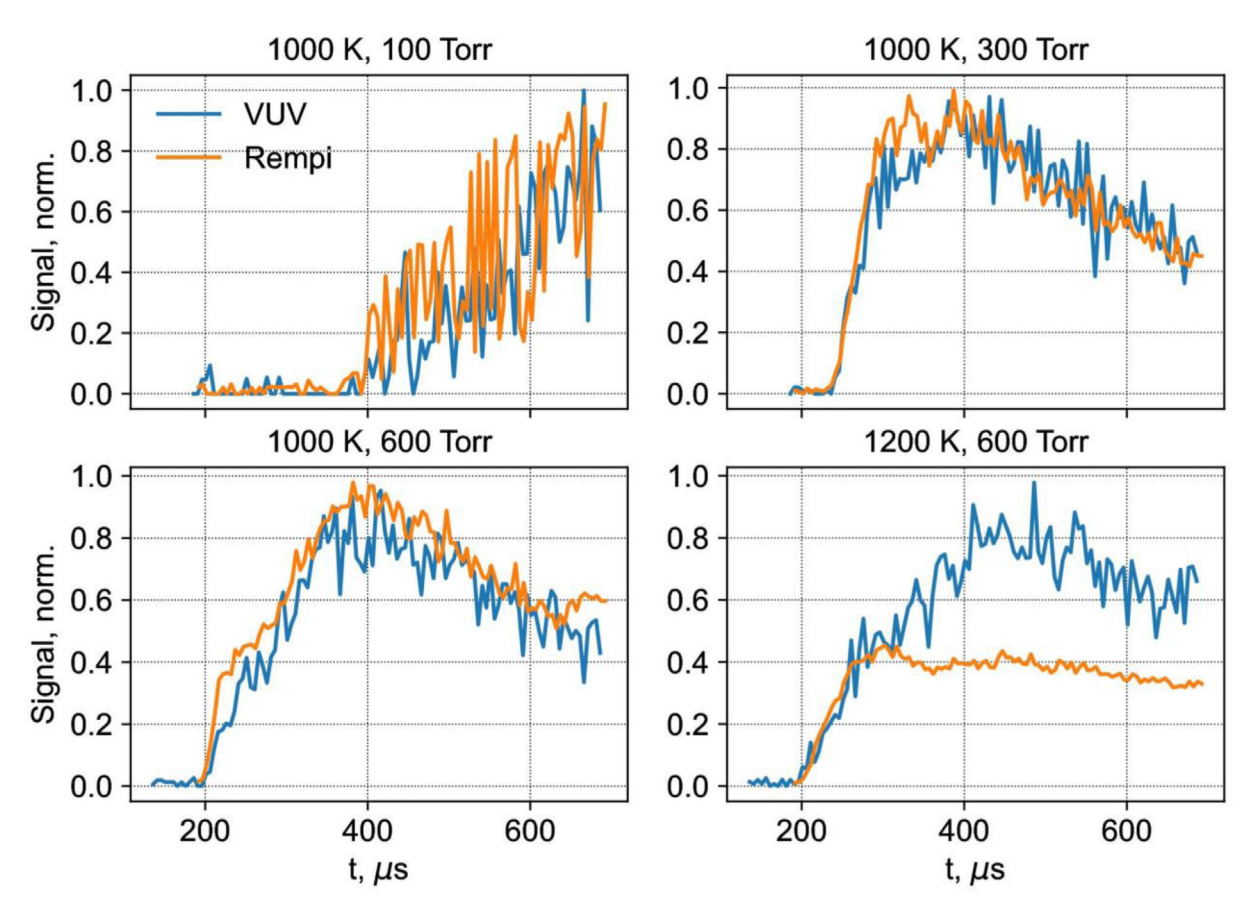


Figure 9. Selected temporal profiles of the m/z = 128 signal in the pyrolysis of nitrosobenzene/acetylene mixtures, comparing one-photon VUV ionization at 118 nm (blue trace) and 1 + 1 REMPI photoionization at 278.5 nm (orange trace). Traces in top and lower left panels (1000 K, 100-600 Torr) show agreement between the shapes of REMPI and VUV data, suggesting formation of a single C<sub>10</sub>H<sub>8</sub> isomer. The differing temporal shapes in the lower right panel (1200 K, 600 Torr) suggest variations in the isomeric composition of  $C_{10}H_8$  between the early and late stages of the gas pulse, reflecting distinct detection sensitivities of VUV and REMPI ionization schemes for different isomers.

### 4. Conclusions

While pulse-mode high-temperature microreactors have been employed in prior studies, [28,36,37] the transient gas dynamics of variable-flow-rate pulsed systems remained unexplored due to their complexity. Although theoretical work addressed nonstationary flows,<sup>[38,39]</sup> experimental characterization was lacking. In this work, we used the temporal shapes of signals to learn about the nature of the gas flow in the pulsed microreactor. Thus, from the gas velocity estimations derived from transit times, it was found that depending on backing pressure, the microreactor exhibits either subsonic (p = 100 Torr) or supersonic (p = 300-600 Torr) flow. This finding was additionally validated by the CFD simulations. Additionally, we found that at  $p \ge 300$  Torr, signal rise times matched valve opening times, confirming uniform gas velocity and flow-rate-proportional pressure changes, thus simplifying kinetic analysis. It was also revealed from the time profiles of nitrosobenzene signals at p = 600 Torr that centerline-to-wall temperature gradients exist, indicating incomplete heating of the gas at higher pressure during its transit through the heated zone.

Under our experimental conditions, phenyl radicals produced via nitrosobenzene pyrolysis primarily yield phenylacetylene (C<sub>8</sub>H<sub>6</sub>) and naphthalene (C<sub>10</sub>H<sub>8</sub>). The pressure- and temperaturedependent product distributions align with HACA-mediated pathways. At high temperatures, the classic Frenklach HACA mechanism (Figure 2) dominates, favoring phenylacetylene formation. At low temperatures and high pressures, the C<sub>8</sub>H<sub>7</sub> (C<sub>6</sub>H<sub>5</sub>C<sub>2</sub>H<sub>2</sub>) intermediate stabilizes, enabling two competing HACA routes (Figures 3,4) to outpace the original mechanism. Naphthalene production exhibits a nonmonotonic temperature dependence, peaking at 800 K before declining at higher temperatures. Its formation is also strongly pressure-sensitive: at 800 K, naphthalene accounts for 53% of the product yield at 300 Torr, but only 10% at 100 Torr, underscoring the role of collisional stabilization in promoting secondary HACA pathways.

Finally, the m/z = 128 signals measured via two independent techniques (VUV and REMPI photoionization) exhibit strong correlation under most experimental conditions, confirming their correspondence to naphthalene. However, discrepancies emerge exclusively at high pressures (600 Torr) and temperatures (1,200 K) (Figure 9) and are localized to the "white zone," where vinylacetylene concentrations are elevated (Figure 7). We attribute this divergence to a competing pathway: under these extreme conditions, phenyl radicals react with vinylacetylene, forming a C<sub>10</sub>H<sub>9</sub> intermediate. At high temperatures, this complex decomposes into one-ring aromatic compounds (1- and/or 4-phenylvinylacetylene  $(C_6H_5(CH)_2C_2H / C_6H_5C_2C_2H_3, C_{10}H_8))$ ,

Chemistry Europe

European Chemical Societies Publishing

isomeric to naphthalene.<sup>[35]</sup> These isomers exhibit distinct photoionization efficiencies in VUV versus REMPI, explaining the observed disparities in temporal signal profiles.

## **Supporting Information**

Details of computational fluid dynamics (CFD) simulations: Step 1 – wall temperature profile simulation, Step 2 – valve cycle CFD simulation; CFD analysis of microreactor conditions; Microreactor construction; Figures S1–S6; Semi-quantitative analysis of the m/z=28 signal; Excel file ESI containing experimentally measured ion counts at various m/z and different inlet pressures, temperatures, and delay times.

## **Acknowledgments**

This work was supported by the Russian Science Foundation (grant number 25–69–00068).

#### **Conflict of Interest**

The authors declare no conflict of interest.

## **Data Availability Statement**

The data that support the findings of this study are available from the corresponding author upon reasonable request.

**Keywords:** gas-phase reactions  $\cdot$  HACA mechanism  $\cdot$  high-temperature microreactor  $\cdot$  PAH formation  $\cdot$  radical reactions

- G. Wenzel, I. R. Cooke, P. B. Changala, E. A. Bergin, S. Zhang, A. M. Burkhardt, A. N. Byrne, S. B. Charnley, M. A. Cordiner, M. Duffy, Z. T. P. Fried, H. Gupta, M. S. Holdren, A. Lipnicky, R. A. Loomis, H. T. Shay, C. N. Shingledecker, M. A. Siebert, D. A. Stewart, R. H. J. Willis, C. Xue, A. J. Remijan, A. E. Wendlandt, M. C. McCarthy, B. A. McGuire, Science 2024, 386, 810.
- [2] V. Lannuque, K. Sartelet, Atmos. Chem. Phys. 2024, 24, 8589.
- [3] C. Ao, J. Yan, T. Yan, L. Zhang, P. Wang, Combust. Flame 2024, 259, 113183.
- [4] V. Krasnoukhov, P. Pivovarov, M. Zagidullin, V. Azyazov, A. Mebel, A. Morozov, Astron. Rep. 2022, 66, 811.
- [5] M. S. Murga, *Uspekhi Fiz. Nauk* **2024**, *194*, 1017.
- [6] R. I. Kaiser, N. Hansen, J. Phys. Chem. A 2021, 125, p. 3826.
- [7] A. M. Mebel, Y. Georgievskii, A. W. Jasper, S. J. Klippenstein, Proc. Combust. Inst. 2017, 36, 919.
- [8] M. Frenklach, D. W. Clary, W. C. Gardiner Jr, S. E. Stein, in Symposium (International) on Combustion, 1985, 20, Elsevier, 887–901.

- [9] M. Frenklach, H. Wang, in Symposium (International) on combustion, 1991, 23, Elsevier, 1559–1566.
- [10] H. Wang, M. Frenklach, J. Phys. Chem. 1994, 98, 11465.
- [11] J. Bittner, J. Howard, in Symposium (International) on Combustion, 1981, 18, Elsevier, 1105–1116.
- [12] N. W. Moriarty, N. J. Brown, M. Frenklach, J. Phys. Chem. A 1999, 103, 7127.
- [13] M. Frenklach, N. W. Moriarty, N. J. Brown, in *Symposium (International) on Combustion*, 1998, 27, Elsevier, 1655–1661.
- [14] H. Richter, O. A. Mazyar, R. Sumathi, W. H. Green, J. B. Howard, J. W. Bozzelli, J. Phys. Chem. A 2001, 105, 1561.
- [15] I. Tokmakov, M.-C. Lin, J. Am. Chem. Soc. 2003, 125, 11397.
- [16] V. Kislov, N. Islamova, A. Kolker, S. Lin, A. Mebel, J. Chem. Theory Comput. 2005, 1, 908.
- [17] Y. Georgievskii, S. J. Klippenstein, J. Phys. Chem. A 2003, 107, 9776.
- [18] A. Fahr, S. Stein, in *Symposium (International) on Combustion*, **1989**, *22*, Elsevier. 1023–1029.
- [19] T. Yu, M.-C. Lin, C. Melius, Int. J. Chem. Knetics 1994, 26, 1095.
- [20] T. Yu, M.-C. Lin, J. Am. Chem. Soc. 1993, 115, 4371.
- [21] D. S. Parker, R. I. Kaiser, T. P. Troy, M. Ahmed, Angew. Chem., Int. Ed. 2014, 53, 7740.
- [22] T. Yang, T. P. Troy, B. Xu, O. Kostko, M. Ahmed, A. M. Mebel, R. I. Kaiser, Angew. Chem., Int. Ed. 2016, 55, 14983.
- [23] T.-C. Chu, Z. J. Buras, M. C. Smith, A. B. Uwagwu, W. H. Green, *Phys. Chem. Chem. Phys.* 2019, 21, 22248.
- [24] D. Proch, T. Trickl, Rev. Sci. Instrum. 1989, 60, 713,.
- [25] J. Gray, J. Bossert, Y. Shyur, B. Saarel, T. Briles, H. Lewandowski, J. Chem. Phys. 2021, 154, 024201.
- [26] R. M. Stephenson, Handbook of the thermodynamics of organic compounds. Springer Science & Business Media, 2012.
- [27] M. V. Zagidullin, R. I. Kaiser, D. P. Porfiriev, I. P. Zavershinskiy, M. Ahmed, V. N. Azyazov, A. M. Mebel, J. Phys. Chem. A 2018, 122, 8819.
- [28] Q. Guan, K. N. Urness, T. K. Ormond, D. E. David, G. B. Ellison, J. W. Daily, Int. Rev. Phys. Chem. 2014, 33, 447.
- [29] Y. Zhang, J. Cai, L. Zhao, J. Yang, H. Jin, Z. Cheng, Y. Li, L. Zhang, F. Qi, Combust. 8778876231YTFlame 2012, 159, 905.
- [30] M. C. Smith, G. Liu, Z. J. Buras, T.-C. Chu, J. Yang, W. H. Green, J. Phys. Chem. A 2020, 124, 2871.
- [31] V. D. Knyazev, S. I. Stoliarov, I. R. Slagle, Symp. (Int.) Combust. 1996, 26, 513.
- [32] T. Adam, R. Zimmermann, Anal. Bioanal. Chem. 2007, 389, 1941.
- [33] Z. Zhou, M. Xie, Z. Wang, F. Qi, Rapid Commun. Mass Spectrom.: Int. J. Devoted Rapid Dissem. Up-to-the-Minute Res. Mass Spectrom. 2009, 23, 3994.
- [34] Y. Y. Li, J. Z. Yang, Z. J. Cheng, "Photonionization Cross Section Database." http://flame.nsrl.ustc.edu.cn/database/(accessed).
- [35] L. Zhao, R. I. Kaiser, B. Xu, U. Ablikim, M. Ahmed, M. V. Zagidullin, V. N. Azyazov, A. H. Howlader, S. F. Wnuk, A. M. Mebel, J. Phys. Chem. Lett. 2018, 9, 2620.
- [36] G. T. Buckingham, T. K. Ormond, J. P. Porterfield, P. Hemberger, O. Kostko, M. Ahmed, D. J. Robichaud, M. R. Nimlos, J. W. Daily, G. B. Ellison, J. Chem. Phys. 2015, 142, 044307.
- [37] A. M. Scheer, C. Mukarakate, D. J. Robichaud, M. R. Nimlos, H.-H. Carstensen, G. Barney Ellison, J. Chem. Phys. 2012, 136, 044309.
- [38] F. Sharipov, Vacuum 2013, 90, 25.
- [39] E. Shakhov, V. Titarev, Vacuum 2014, 109, 284.

Manuscript received: August 5, 2025 Revised manuscript received: September 6, 2025 Version of record online: September 24, 2025